Editors' Suggestion

Double accumulation and anisotropic transport of magnetoelastic bosons in yttrium iron garnet films

Pascal Frey [1,*] Dmytro A. Bozhko [2,†] Victor S. L'vov [3,‡] Burkard Hillebrands [1,§] and Alexander A. Serga [1,‖]

[1] *Fachbereich Physik and Landesforschungszentrum OPTIMAS, Technische Universität Kaiserslautern, 67663 Kaiserslautern, Germany*

[2] *Department of Physics and Energy Science, University of Colorado Colorado Springs, Colorado Springs, Colorado 80918, USA*

[3] *Department of Chemical and Biological Physics, Weizmann Institute of Science, Rehovot 76100, Israel*

(Received 18 March 2021; revised 29 June 2021; accepted 1 July 2021; published 19 July 2021)

Interaction between quasiparticles of a different nature, such as magnons and phonons in a magnetic medium, leads to the mixing of their properties and the formation of hybrid states in the areas of intersection of individual spectral branches. We recently reported the discovery of a new phenomenon mediated by the magnon-phonon interaction: the spontaneous bottleneck accumulation of magnetoelastic bosons under electromagnetic pumping of pure magnons into a ferrimagnetic yttrium iron garnet film. Here, by studying the transport properties of the accumulated magnetoelastic bosons, we reveal that such accumulation occurs in two frequency-distant groups of quasiparticles: quasiphonons and quasimagnons. They propagate with different velocities in different directions relative to the magnetization field. The theoretical model we propose qualitatively describes the double accumulation effect, and the analysis of the two-dimensional spectrum of quasiparticles in the hybridization region allows us to determine the wave vectors and frequencies of each of the groups.

DOI: 10.1103/PhysRevB.104.014420

I. INTRODUCTION

The physics of quasiparticles constitutes a very prominent research field over the last decade [1]. Especially magnons and phonons—the quanta of spin waves [2] and lattice vibrations [3]—have been extensively studied within the solid state research domain. In the early days, these two systems were usually consider to be noninteracting. Subsequently, the emphasis shifted to a full description of the solid-state system and the study of related subsystems [4–12]. The variety of interactions between these two subsystems creates a wide range of applications [13] exploiting the fact that in magnetostrictive materials the mechanical stress affects the magnetization orientation and vice versa [14–21]. For instance, the mechanical stress produced by an acoustic wave can drive magnetization dynamics and excite magnons in such materials if the frequency of lattice vibrations matches the eigenexcitations of the spin system [22,23]. Furthermore, hybrid waves [24–27] with mixed magnonic and phononic features [28–32] also exist. The corresponding quasiparticles are called magnetoelastic bosons [33] or magnon polarons [11,34–37]. Due to their mixed hybrid state between phonons and magnons, they are capable of carrying spin information at velocities close to those of phonons. This is currently attracting much attention to these quasiparticles as promising data carriers for future applications in spintronics [29,30,38–40]. In particular, the spontaneous bottleneck accumulation of hybrid magnetoelastic quasiparticles with rather high group velocities was recently discovered in an overpopulated magnon gas in yttrium iron garnet (YIG) films [33].

In this paper, we report measurements of the two-dimensional transport properties of the accumulated quasiparticles using space- and time-resolved Brillouin light scattering (BLS) spectroscopy. We show that the accumulation process leads to the appearance of two—slow and fast—groups of quasiparticles, represented by the blue and red dots in the black dashed square in Fig. 1, propagating in distinctly different directions. The slow group, indicated by the blue dot, has a frequency slightly higher than that of the magnon Bose-Einstein condensate (BEC) [41,42] formed at the bottom of the spin-wave spectrum. The frequency of the fast group of hybrid bosons, shown by the red dot, is lower than the BEC frequency.

We also present an analytical model that accounts for the details of the relaxation dynamics in the presence of a nonzero BEC frequency minimum including variation of the scattering coefficient in the region of the avoided crossing between phonon and magnon branches. The model qualitatively explains the observed phenomenon of double accumulation and the spectral positions of the two quasiparticle groups.

Our analysis of the two-dimensional hybrid frequency spectra quantitatively relates the values and directions of quasiparticle velocities to the formation of caustic beams [43,44] in the spatial distribution of the quasiparticle density. The presented findings will potentially allow to control the characteristics of the accumulated quasiparticles and manipulate their behavior for information transfer and processing [45–47].

The paper is organized as follows. The experimental setup is described in Sec. II A. In Sec. II B, the experimental results on propagation velocities of the slow and fast quasiparticle packets are presented. In Sec. III, we refer to the

*pfrey@rhrk.uni-kl.de
†dbozhko@uccs.edu
‡victor.lvov@gmail.com
§hilleb@physik.uni-kl.de
‖serga@physik.uni-kl.de

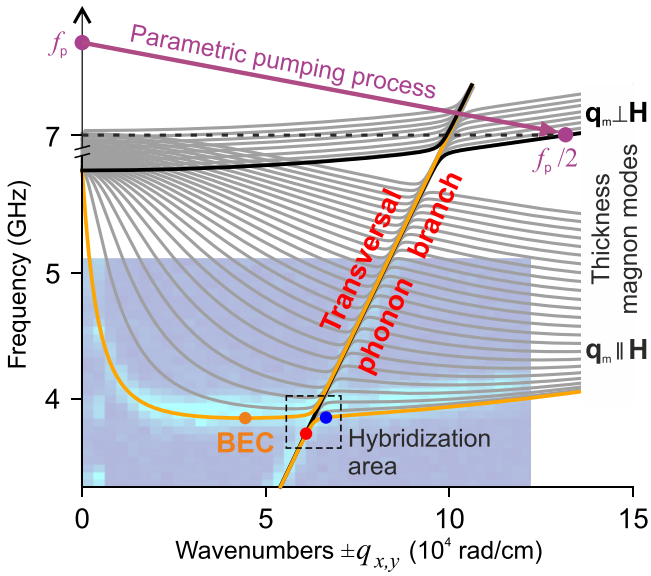

FIG. 1. A magnon-phonon hybrid spectrum of an in-plane magnetized 5.6-μm-thick YIG film calculated for wave vectors $\pm q_x$ and $\pm q_y$ oriented along and perpendicular to the bias magnetic field, respectively. The hybridization with the transversal phonon branch is shown for an external magnetic field of $\mu_0 H = 135$ mT. The weaker coupled longitudinal phonon branch is neglected. The violet arrow indicates the parallel parametric pumping process in the $\boldsymbol{q}_m \perp \boldsymbol{H}$ magnon branch using microwave photons of frequency f_p. The population of the pumped magnons at frequency $f_p/2$ (purple dot) thermalizes over the spin-wave spectrum via four-magnon scattering processes. The thermalization process leads to the accumulation of magnetoelastic quasiparticles within the magnon-phonon hybridization area (dashed square) and magnon Bose-Einstein condensation at the bottom of the spin-wave spectra (green dot). The blue and red dots mark the spectral positions of the measured hybrid quasiparticles. The color map shows the thermal magnon-phonon density distribution measured by means of frequency- and wave-vector-resolved Brillouin light scattering spectroscopy.

basics of magnon-phonon hybridization theory by deriving a hybridized magnon-phonon Hamiltonian in Sec. III A and presenting a statistical description of magnetoelastic modes in Sec. III B. The model of double accumulation of hybrid bosons is presented in Sec. IV, where we introduce a one-dimensional differential model in Sec. IV A, estimate the scattering rates within and between the quasiparticle spectral branches in Sec. IV B, and solve the rate equations above and below the BEC frequency in Secs. IV C and IV D, respectively. Analysis of the experimental data based on the theory of caustic magnon transport in Sec. V allows us to determine frequencies and wave vectors of the two groups of hybrid quasiparticles. In Sec. VI, we discuss and summarize the obtained results.

II. EXPERIMENT

A. Setup

We studied the process of spontaneous accumulation of hybrid quasiparticles and determined their properties by means of BLS spectroscopy [48]. The sample is illuminated by focused laser light with a wavelength of 532 nm. Due to inelastic scattering processes, a photon can absorb or excite a magnon and therefore gain (anti-Stokes process) or lose energy (Stokes process). Thus, the intensities of the Stokes and anti-Stokes spectral peaks are proportional to the density of quasiparticles. The backward scattered light is collected and directed to a tandem Fabry-Pérot interferometer, where its frequency spectrum is analyzed with a resolution of about 100 MHz. By carefully selecting the incident angle α_x of the laser light along the external magnetic field we achieve a wave-vector selection (see Fig. 2) [49,50]. The linear response function of the BLS setup in the wave-vector plane (q_x, q_y) follows a Gaussian distribution and consequently limits the wave-vector resolution with a standard deviation of $\sigma = 1500$ rad/cm. To freely move the sample along all three spatial dimensions it is mounted on a motorized linear stage system. Additionally, a time-resolution system with a resolution of 400 ps is combined with the interferometer and a pulsed microwave source [51]. Therefore the setup is able to perform frequency-, wave-vector-, time-, and space-resolved scans [52].

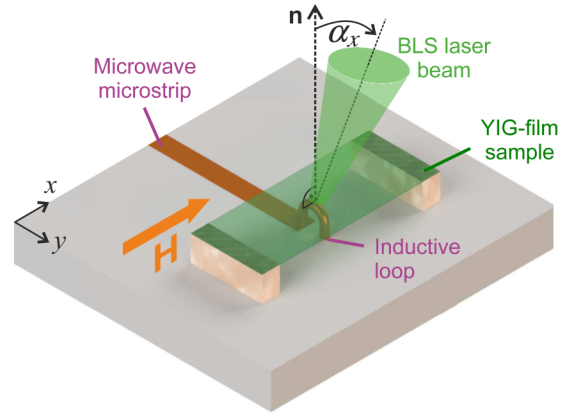

FIG. 2. Sketch of the experimental setup. The microwave part consist of a microwave stripline, which blends into a half-loop with its plane oriented perpendicular to the sample surface and the external magnetic field $\boldsymbol{H}$. The sample is mounted on top of two distant holders in such a way that the center of the sample is located above the excitation loop. The sample itself consists of a YIG film of 5.6-μm thickness grown on a GGG substrate (500 μm) and covered by a thin dielectric mirror coating (<1 μm). The magnons in the YIG film are detected via inelastic laser light scattering ($\lambda = 532$ nm) measured by a tandem Fabry-Pérot interferometer. The value of an incident angle α_x of the probing laser beam in the (x, z) plane defines the measured wave vector q_x oriented along the magnetic field.

The measurements are carried out at room temperature in a single-crystal yttrium iron garnet (YIG: $Y_3Fe_5O_{12}$) sample. This ferrimagnetic material was chosen for the experiment because it uniquely combines extremely low damping of magnetic and elastic excitations [53]. The sample is a piece of 5.6-μm-thick YIG film grown by liquid phase epitaxy on top of a 500-μm-thick gadolinium gallium garnet (GGG: $Gd_3Ga_5O_{12}$) substrate in (111) crystallographic plane (see Fig. 2). Micron-thick YIG films as well as GGG substrates are transparent to green light and thus make BLS probing of magnon-phonon hybrid waves possible. The probing light beam is focused onto the YIG film through the GGG substrate. To ensure homogeneous reflection of the probing light from

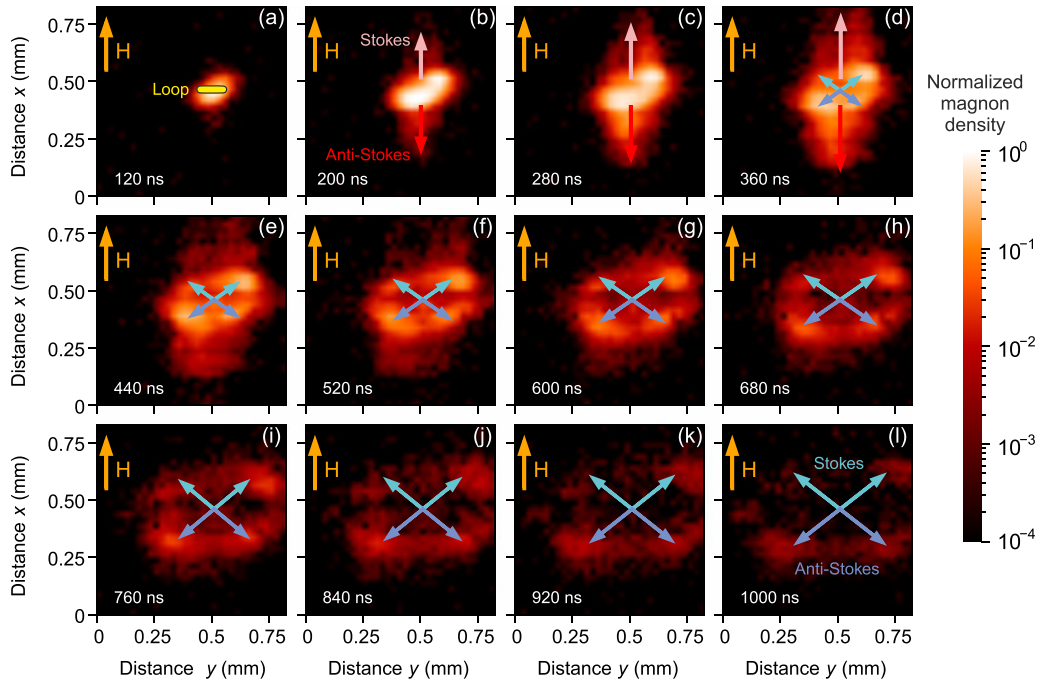

FIG. 3. Spatial distribution of the BLS-signal intensity corresponding to the distribution of the quasiparticle density for different times from the moment in time the pump pulse is turned on. The propagation of two groups of quasiparticles is visible. The magnon-phonon hybrid packets propagate away from the excitation loop in six directions. The data are generated by integration over the 300 MHz frequency range of the BLS signal. Each of the shown density distributions summarizes the BLS experiment's Stokes ($+q_x$) and anti-Stokes ($-q_x$) signals.

the YIG-film surface and thus uniform spatial sensitivity of the BLS setup, YIG is covered with a thin dielectric mirror coating created with a SiO_2/TiO_2 bilayer structure (< 1 μm). The mirror reflects over 90 % light at 532 nm.

Magnons are excited in the in-plane magnetized YIG sample by microwave electromagnetic pumping via the parallel parametric pumping process. In such a process [54], one microwave photon of the pumping frequency f_p splits into two magnons with opposite wave vectors $\pm\boldsymbol{q}_m$ and each the frequency $f_p/2$. Due to the choice of the values of the bias magnetic field $\mu_0 H = 135$ mT and the pumping frequency $f_p = 14$ GHz, the parametrically excited magnons are injected (see violet arrow in Fig. 1) into the transverse branch ($\boldsymbol{q}_m \perp \boldsymbol{H}$) of the spin-wave frequency spectrum [55] at a distance of about 2 GHz above the bottom of the spectrum.

In this experiment, it is essential to perform two-dimensional transport measurements, which are impossible with a microstrip pump resonator used in our previous experiments [33,56]. Therefore the resonator is replaced by a half-loop antenna with a diameter of 100 μm (see Fig. 2) to create a two-dimensional spatially localized pumping microwave field. The half-loop is made of a gold wire with a diameter of 25 μm and is shorted to the ground of the microstrip line that feeds the pumping power to it. Since the quality factor of this antenna is unity, the pumping power required to reach a pronounced accumulation of hybrid quasiparticles and the Bose-Einstein condensation of magnons is about 600 W. This power is applied during a 200-ns-long excitation pulse. To ensure that no additional heating effects influence the measurements, the excitation pulse is followed by a 250-μs idle time, where the magnons can decay and the created heat can dissipate into the surroundings.

B. Experimental results

The measurement cycle begins at $t = 0$, when the pumping power is switched on and when a microwave pulse begins to inject magnons into the system. From thereon the magnon gas is formed and it thermalizes via four-magnon scattering processes [42,54]. The thermalization process causes an increase in the local chemical potential of the injected magnon gas in the vicinity of the frequency minimum. As soon as it reaches the minimum of the magnon frequency, a magnon BEC forms at the spot marked by the blue dot in Fig. 1.

Another cluster of quasiparticles is formed at the intersection of the phonon and magnon branches [33]. Quasiparticles belonging to this cluster are in hybrid states between phonons and magnons, combining the properties of both. Due to the rather small size of the hybridization region in the frequency and wave-vector space, the BLS setup is not able to differentiate the population of quasiparticles within the magnetoelastic interaction region. However, time-resolved measurements of the spatial distribution of these quasiparticles [see Figs. 3(a)–3(l)] reveal the presence of two groups of quasiparticles with significantly different propagation properties.

Figure 3(a) depicts the beginning of quasiparticle accumulation in real space in the vicinity of the pump loop at time $t = 120$ ns after the start of pumping. Here, the loop position is shown by the gold segment. During the pumping pulse ($t \leqslant 200$ ns) the number of particles in the hybridization region rises [see Figs. 3(a) and 3(b)], and two beams of quasiparticles start to travel upward and downward along the direction of the external magnetic field $\boldsymbol{H}$ as shown in Figs. 3(b) and 3(c). The slightly red arrows mark the Stokes data, indicating the quasiparticles propagating with a positive wave

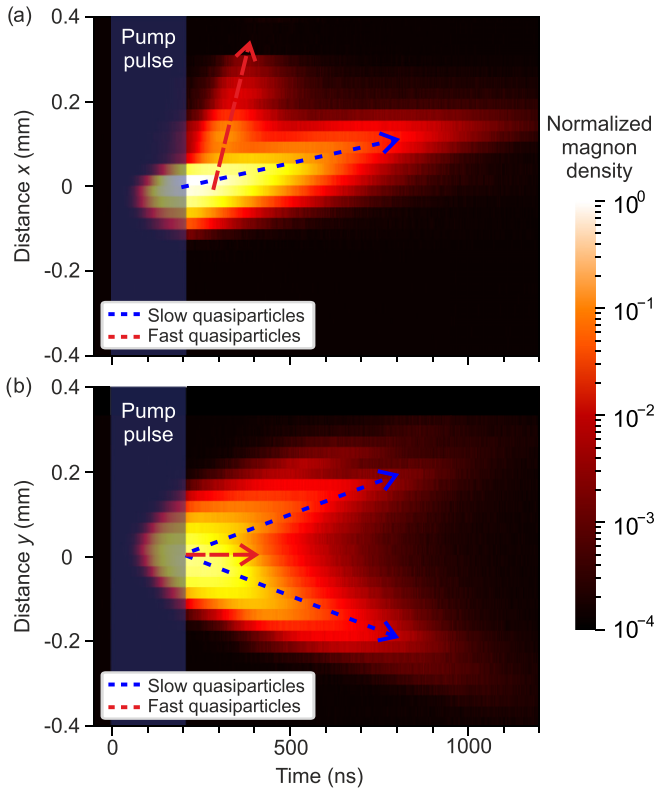

FIG. 4. Space-time diagrams along the x and y axes in the film plane for packets of fast and slow quasiparticles, which correspond to Stokes components of the BLS signals and thus have positive values of wave vectors q_x. The blue and red dashed lines show a linear temporal fit of the positions of these packets. Two packets of quasiparticles with wave vectors $\pm q_y$ propagate with the same speed in opposite directions along the y axis, and two packets – along the x axis with different speeds.

vector of $q = q_{\text{fast}}$, while the red arrows for anti-Stokes data correspond to the quasi particles propagating with a negative wave vector $q = -q_{\text{fast}}$.

Beginning at $t = 360$ ns [see Fig. 3(d)], four additional magnon packets propagate obliquely to the external magnetic field as it is marked by two white and two blue arrows in Figs. 3(e-l)]. The speed of their propagation is approximately ten times lower than the speed of propagation of quasiparticle packets along the field. Hereinafter we will refer to these two groups of quasiparticles as fast and slow ones.

To analyze the propagation process of the fast and slow packets, a center-of-mass algorithm tracks the path of each of those packets individually. The space-time diagrams for the fast and slow packets in x and y directions are shown in Figs. 4(a) and 4(b). The packets positions $\boldsymbol{R}(t) = \{X(t), Y(t)\}$, represented by the red and blue arrows, are found by the two-dimensional linear in time fitting process $\boldsymbol{R}(t) = \boldsymbol{v}t + \boldsymbol{R}_0$ with the Levenberg-Marquardt algorithm [57]:

$$v_{\text{slow}} \approx (368 \pm 2)\ \text{m/s}, \quad \alpha_{\text{slow}} \approx 59^\circ \pm 0.3^\circ, \tag{1a}$$

$$v_{\text{fast}} \approx (3070 \pm 207)\ \text{m/s}, \quad \alpha_{\text{fast}} \approx 0^\circ \pm 0^\circ. \tag{1b}$$

We see that the velocity of the slow quasiparticle group is higher than that of pure magnons (≈90 m/s) with wave vectors corresponding to the hybridization region, while the velocity of the fast group is lower than that of pure phonons (≈ 3850 m/s in bulk YIG). This comparison of velocity values allows us to approximately localize the spectral positions of the fast and slow quasiparticles in the hybridization region–indicated by the red and blue dots inside the black dashed box in Fig. 1. It can be assumed that the slow quasiparticles are mainly of magnonic nature with a small contribution of phononic admixture. In turn, the fast quasiparticles predominantly consist of phonons with a small magnonic contribution. Particularly remarkable is the absence of the population of quasiparticle states between these two—quasimagnon and quasiphonon—extreme cases. Because of close spectral positions of the quasimagnon and quasiphonon states, such selective population is difficult to explain by some features of scattering of parametrically pumped magnons far from the bottom of the spin-wave spectrum. Thus, to understand the observed phenomenon of the double quasiparticle accumulation, a theoretical analysis of the situation near the magnon-phonon hybridization region is required. It is presented in the following sections.

III. MAGNON-PHONON HYBRIDIZATION BACKGROUND

The goal of this section is to recall the Hamiltonian description of interacting magnons and photons in the vicinity of cross-section of their frequency spectra [54,58], required for further discussion of our experimental finding. Some details on statistical descriptions of resulting magnetoelastic modes can be found in Appendix of Ref. [59].

A. Hybridized magnon-phonon Hamiltonian

At high temperatures, we can restrict ourselves to the classical limit and describe the system of interacting magnons and phonons in the framework of a classical Hamiltonian formalism. This approach is applicable to a wide class of weakly interacting wave systems, allowing a physically transparent and very compact description of their common properties, see, for instance, Chap. 1 in Ref. [54] and in more detail in Ref. [58].

Introducing complex canonical amplitudes of magnons and phonons in the wave-vector $\boldsymbol{q}$ representation, $a(\boldsymbol{q}, t) \equiv a_{\boldsymbol{q}}$ and $b(\boldsymbol{q}, t) \equiv b_{\boldsymbol{q}}$ we can write their Hamiltonian equation of motion as follows:

$$i\,\frac{\partial a_{\boldsymbol{q}}}{\partial t} = \frac{\partial \mathcal{H}}{\partial a^*_{\boldsymbol{q}}}, \quad i\,\frac{\partial b_{\boldsymbol{q}}}{\partial t} = \frac{\partial \mathcal{H}}{\partial b^*_{\boldsymbol{q}}}. \tag{2a}$$

Here, the Hamiltonian function $\mathcal{H}$ (hereafter referred to as"the Hamiltonian" for brevity) is a functional of the canonical variables $a_{\boldsymbol{q}}$, $b_{\boldsymbol{q}}$ for all $\boldsymbol{q}$ and their complex conjugated counterparts $a^*_{\boldsymbol{q}}$, $b^*_{\boldsymbol{q}}$. We chose $\mathcal{H}$ as

$$\mathcal{H} = \mathcal{H}_2 + \mathcal{H}_4, \tag{2b}$$

$$\mathcal{H}_2 = \sum_{\boldsymbol{q}} [\omega^{\text{m}}_{\boldsymbol{q}} a_{\boldsymbol{q}} a^*_{\boldsymbol{q}} + \omega^{\text{p}}_{\boldsymbol{q}} b_{\boldsymbol{q}} b^*_{\boldsymbol{q}} + \frac{\Delta_\omega}{2}(a_{\boldsymbol{q}} b^*_{\boldsymbol{q}} + a^*_{\boldsymbol{q}} b_{\boldsymbol{q}})], \tag{2c}$$

$$\mathcal{H}_4 = \frac{1}{4} \sum_{\boldsymbol{q}_1+\boldsymbol{q}_2=\boldsymbol{q}_3+\boldsymbol{q}_4} T_{\mathbf{12,34}}\, a^*_{\mathbf{1}} a^*_{\mathbf{2}} a_{\mathbf{3}} a_{\mathbf{4}}, \quad a_{\boldsymbol{j}} \equiv a_{\boldsymbol{q}_j}. \tag{2d}$$

The first two terms in $\mathcal{H}_2$ describe the free propagation of magnons and phonons with the dispersion laws $\omega_{\boldsymbol{q}}^{\mathrm{m}}$ and $\omega_{\boldsymbol{q}}^{\mathrm{p}}$, respectively. The last two terms in $\mathcal{H}_2$ are responsible for their linear coupling due to the magnetoelastic effect with a coupling amplitude $\Delta_\omega = 2\pi\,\Delta_{\mathrm{f}} = 2\pi \times 98$ MHz [10,60]. In the acoustic system nonlinearity can be safely neglected in comparison with the strongly nonlinear spin-wave (magnon) subsystem.

Without interaction, the dispersion laws $\omega_{\boldsymbol{q}}^{\mathrm{m}}$ and $\omega_{\boldsymbol{q}}^{\mathrm{p}}$ will cross at some hybridization wave vector $\boldsymbol{q} = \boldsymbol{q}_\times : \omega_{\boldsymbol{q}_\times}^{\mathrm{m}} = \omega_{\boldsymbol{q}_\times}^{\mathrm{p}} = \omega_\times$, as seen in Fig. 1. Here, we consider a weak coupling regime with a narrow hybridization region δq around $\boldsymbol{q}_\times$, such that

$$\Delta_\omega \equiv \delta q \frac{\partial\left(\omega_{\boldsymbol{q}_\times}^{\mathrm{p}} - \omega_{\boldsymbol{q}_\times}^{\mathrm{m}}\right)}{\partial q} \ll \omega_\times \,. \tag{3}$$

Being interested in the system evolution in the hybridization region δq, we can restrict ourselves to the four-magnon interaction Hamiltonian $\mathcal{H}_4$, Eq. (2d) [54] with the sum restricted by the hyper-surface $\boldsymbol{q}_1 + \boldsymbol{q}_2 = \boldsymbol{q}_3 + \boldsymbol{q}_4$. The interaction amplitude $T_{\mathbf{12,34}}$ depends on $\boldsymbol{q}_1, \boldsymbol{q}_2, \boldsymbol{q}_3$, and $\boldsymbol{q}_4$.

The quadratic Hamiltonian $\mathcal{H}_2$ can be diagonalized by the linear canonical Bogoliubov (u, v) transformation of the form

$$\begin{aligned} a_{\boldsymbol{q}} &= c_{\boldsymbol{q}}^{\mathrm{L}} \cos\varphi_{\boldsymbol{q}} + c_{\boldsymbol{q}}^{\mathrm{U}} \sin\varphi_{\boldsymbol{q}}, \\ b_{\boldsymbol{q}} &= -c_{\boldsymbol{q}}^{\mathrm{L}} \sin\varphi_{\boldsymbol{q}} + c_{\boldsymbol{q}}^{\mathrm{U}} \cos\varphi_{\boldsymbol{q}}, \end{aligned} \tag{4a}$$

in which the coordinate system rotation angle $\varphi_{\boldsymbol{q}}$ is chosen as follows:

$$\cos^2\varphi_{\boldsymbol{q}} = \frac{1}{2}\left[1 + \frac{O_{\boldsymbol{q}}}{\left(1+O_{\boldsymbol{q}}^2\right)^{1/2}}\right],\ O_{\boldsymbol{q}} = \frac{\omega_{\boldsymbol{q}}^{\mathrm{p}} - \omega_{\boldsymbol{q}}^{\mathrm{m}}}{\Delta_\omega} \,. \tag{4b}$$

Here, O_q is the dimensionless frequency distance from the crossover. This transformation leads to a new diagonal Hamiltonian $\widetilde{\mathcal{H}}_2$ in terms of new normal canonical amplitudes of the upper (U) and lower (L) magnetoelastic modes (MEMs) $c_{\boldsymbol{q}}^{\mathrm{U}}$ end $c_{\boldsymbol{q}}^{\mathrm{L}}$ with frequencies $\Omega_{\boldsymbol{q}}^{\mathrm{U}}$ and $\Omega_{\boldsymbol{q}}^{\mathrm{L}}$:

$$\widetilde{\mathcal{H}}_2 = \sum_{\boldsymbol{q}} \left[\Omega_{\boldsymbol{q}}^{\mathrm{U}} c_{\boldsymbol{q}}^{\mathrm{U}} c_{\boldsymbol{q}}^{\mathrm{U}*} + \Omega_{\boldsymbol{q}}^{\mathrm{L}} c_{\boldsymbol{q}}^{\mathrm{L}} c_{\boldsymbol{q}}^{\mathrm{L}*}\right], \tag{5a}$$

$$\Omega_{\boldsymbol{q}}^{\mathrm{U}} = \tfrac{1}{2}\left\{\omega_{\boldsymbol{q}}^{\mathrm{m}} + \omega_{\boldsymbol{q}}^{\mathrm{p}} + \sqrt{\left[\omega_{\boldsymbol{q}}^{\mathrm{m}} - \omega_{\boldsymbol{q}}^{\mathrm{p}}\right]^2 + \Delta_\omega^2}\,\right\}, \tag{5b}$$

$$\Omega_{\boldsymbol{q}}^{\mathrm{L}} = \tfrac{1}{2}\left\{\omega_{\boldsymbol{q}}^{\mathrm{m}} + \omega_{\boldsymbol{q}}^{\mathrm{p}} - \sqrt{\left[\omega_{\boldsymbol{q}}^{\mathrm{m}} - \omega_{\boldsymbol{q}}^{\mathrm{p}}\right]^2 + \Delta_\omega^2}\,\right\}. \tag{5c}$$

As usual, the group velocities of these modes are given by

$$\boldsymbol{v}_{\boldsymbol{q}}^{\mathrm{U,L}} = \frac{d\ \Omega_{\boldsymbol{q}}^{\mathrm{U,L}}}{d\boldsymbol{q}} \,. \tag{5d}$$

The interaction Hamiltonian (2d) in these new variables includes terms $\mathcal{H}_4^{\mathrm{UU}}, \mathcal{H}_4^{\mathrm{LL}}$, responsible for the interactions within the U- and L-MEMs, respectively, and a term $\mathcal{H}_4^{\mathrm{LU}}$, that describs the interaction between them:

$$\mathcal{H}_4^{\mathrm{UU}} = \frac{1}{4} \sum_{\boldsymbol{q}_1+\boldsymbol{q}_2=\boldsymbol{q}_3+\boldsymbol{q}_4} T_{\mathbf{12,34}}^{\mathrm{UU}}\, c_{\mathbf{1}}^{\mathrm{U}*} c_{\mathbf{2}}^{\mathrm{U}*} c_{\mathbf{3}}^{\mathrm{U}} c_{\mathbf{4}}^{\mathrm{U}} \,, \tag{6a}$$

$$T_{\mathbf{12,34}}^{\mathrm{UU}} = T_{\mathbf{12,34}}^{\mathrm{UU}} \sin\varphi_{\mathbf{1}} \sin\varphi_{\mathbf{2}} \sin\varphi_{\mathbf{3}} \sin\varphi_{\mathbf{4}} \,,$$

$$\mathcal{H}_4^{\mathrm{LL}} = \frac{1}{4} \sum_{\boldsymbol{q}_1+\boldsymbol{q}_2=\boldsymbol{q}_3+\boldsymbol{q}_4} T_{\mathbf{12,34}}^{\mathrm{LL}}\, c_{\mathbf{1}}^{\mathrm{L}*} c_{\mathbf{2}}^{\mathrm{L}*} c_{\mathbf{3}}^{\mathrm{L}} c_{\mathbf{4}}^{\mathrm{L}} \,, \tag{6b}$$

$$T_{\mathbf{12,34}}^{\mathrm{LL}} = T_{\mathbf{12,34}}^{\mathrm{LL}} \cos\varphi_{\mathbf{1}} \cos\varphi_{\mathbf{2}} \cos\varphi_{\mathbf{3}} \cos\varphi_{\mathbf{4}} \,,$$

$$\mathcal{H}_4^{\mathrm{LU}} = \frac{1}{4} \sum_{\boldsymbol{q}_1+\boldsymbol{q}_2=\boldsymbol{q}_3+\boldsymbol{q}_4} T_{\mathbf{12,34}}^{\mathrm{LU}} \left[\, c_{\mathbf{1}}^{\mathrm{U}*} c_{\mathbf{2}}^{\mathrm{U}*} c_{\mathbf{3}}^{\mathrm{L}} c_{\mathbf{4}}^{\mathrm{L}} + \mathrm{c.c.}\right],$$

$$T_{\mathbf{12,34}}^{\mathrm{LU}} = T_{\mathbf{12,34}}^{\mathrm{LU}} \sin\varphi_{\mathbf{1}} \sin\varphi_{\mathbf{2}} \cos\varphi_{\mathbf{3}} \cos\varphi_{\mathbf{4}} \,. \tag{6c}$$

Here, "c.c." stands for complex conjugation. The energy and particle fluxes within the U- and L-MEM branches, are proportional to $|T_{\mathbf{12,34}}^{\mathrm{UU}}|^2$ and $|T_{\mathbf{12,34}}^{\mathrm{LL}}|^2$, the energy and particle exchange between modes are proportional to $|T_{\mathbf{12,34}}^{\mathrm{LU}}|^2$.

To illustrate how these objects depend on the frequency near the hybridization crossover, where $\omega_{\boldsymbol{q}}^{\mathrm{m}} = \omega_{\boldsymbol{q}}^{\mathrm{p}}$, we plot them in Fig. 5(b) with the shorthand notations:

$$T_{\boldsymbol{q}}^{\mathrm{UU}} \equiv T_{\boldsymbol{q},\boldsymbol{q};\boldsymbol{q},\boldsymbol{q}}^{\mathrm{UU}} \,,\ T_{\boldsymbol{q}}^{\mathrm{LL}} \equiv T_{\boldsymbol{q},\boldsymbol{q};\boldsymbol{q},\boldsymbol{q}}^{\mathrm{LL}} \,,\ T_{\boldsymbol{q}}^{\mathrm{LU}} \equiv T_{\boldsymbol{q},\boldsymbol{q};\boldsymbol{q},\boldsymbol{q}}^{\mathrm{LU}} \,, \tag{7}$$

as functions of the dimensionless distance to the crossover O_q defined by Eq. (4b).

B. Statistical description of magnetoelastic modes

A statistical description of weakly interacting waves can be obtained [58] in terms of a kinetic equation, shown below for the continuous limit, when the system size L is much larger than the wavelength $2\pi/k$:

$$\frac{\partial n^{\mathrm{L}}(\boldsymbol{q},t)}{\partial t} = \mathrm{St}^{\mathrm{L}}(\boldsymbol{q},t) \,, \quad \frac{\partial n^{\mathrm{U}}(\boldsymbol{q},t)}{\partial t} = \mathrm{St}^{\mathrm{U}}(\boldsymbol{q},t) \,. \tag{8}$$

Here $n_{\boldsymbol{q}}^{\mathrm{L}} = n^{\mathrm{L}}(\boldsymbol{q},t)$ and $n_{\boldsymbol{q}}^{\mathrm{U}} = n^{\mathrm{U}}(\boldsymbol{q},t)$ are the same-time pair correlations of the L- and U-MEMs, defined by

$$\begin{aligned} \left\langle c_{\boldsymbol{q}}^{\mathrm{L}} c_{\boldsymbol{q}'}^{\mathrm{L}} \right\rangle &= \frac{4\pi^2}{L^2}\,\delta(\boldsymbol{q}-\boldsymbol{q}')\, n_{\boldsymbol{q}}^{\mathrm{L}} \,, \\ \left\langle c_{\boldsymbol{q}}^{\mathrm{L}}\, c_{\boldsymbol{q}'}^{\mathrm{L}} \right\rangle &= \frac{4\pi^2}{L^2}\,\delta(\boldsymbol{q}-\boldsymbol{q}')\, n_{\boldsymbol{q}}^{\mathrm{L}} \,, \end{aligned}$$

where $\langle \dots \rangle$ stands for the ensemble averaging. In the classical limit, when the occupation numbers of Bose particles $n_q(\boldsymbol{q},t) \gg 1$, $n(\boldsymbol{q},t) = \hbar n_q(\boldsymbol{q},t)$. In what follows, we discuss only the relevant L-MEM population $n_{\boldsymbol{q}}^{\mathrm{L}}$.

The collision integral $\mathrm{St}^{\mathrm{L}}(\boldsymbol{q},t)$ was found, for instance, in Ref. [58] in the framework of the classical Hamiltonian approach. In the limit of large n_q the result coincides with the quantum kinetic equation, derived from the Golden rule, widely used in quantum mechanics. Accounting for the 2L $\Rightarrow$ 2L and 2L $\Rightarrow$ 2U scattering events, we have

$$\mathrm{St}^{\mathrm{L}}(\boldsymbol{q},t) = \mathrm{St}^{\mathrm{LL}}(\boldsymbol{q},t) + \mathrm{St}^{\mathrm{LU}}(\boldsymbol{q},t) \,, \tag{9a}$$

$$\begin{aligned} \mathrm{St}^{\mathrm{LL}}(\boldsymbol{q},t) = \frac{\pi}{4} \int d\boldsymbol{q}_1 d\boldsymbol{q}_2 d\boldsymbol{q}_3\, \delta(\boldsymbol{q}+\boldsymbol{q}_1-\boldsymbol{q}_2-\boldsymbol{q}_3) \\ \times \delta\left(\Omega_{\boldsymbol{q}}^{\mathrm{L}} + \Omega_{\mathbf{1}}^{\mathrm{L}} - \Omega_{\mathbf{2}}^{\mathrm{L}} - \Omega_{\mathbf{3}}^{\mathrm{L}}\right) \left|T_{\boldsymbol{q}\mathbf{1}\,\mathbf{23}}^{\mathrm{LL}}\right|^2 \\ \times \left[n_{\mathbf{2}}^{\mathrm{L}} n_{\mathbf{3}}^{\mathrm{L}} \left(n_{\boldsymbol{q}}^{\mathrm{L}} + n_{\mathbf{1}}^{\mathrm{L}}\right) - n_{\boldsymbol{q}}^{\mathrm{L}} n_{\mathbf{1}}^{\mathrm{L}} \left(n_{\mathbf{2}}^{\mathrm{L}} + n_{\mathbf{3}}^{\mathrm{L}}\right)\right] \end{aligned} \tag{9b}$$

$$\begin{aligned} \mathrm{St}^{\mathrm{LU}}(\boldsymbol{q},t) = \frac{\pi}{4} \int d\boldsymbol{q}_1 d\boldsymbol{q}_2 d\boldsymbol{q}_3\, \delta(\boldsymbol{q}+\boldsymbol{q}_1-\boldsymbol{q}_2-\boldsymbol{q}_3) \\ \times \delta\left(\Omega_{\boldsymbol{q}}^{\mathrm{U}} + \Omega_{\mathbf{1}}^{\mathrm{U}} - \Omega_{\mathbf{2}}^{\mathrm{L}} - \Omega_{\mathbf{3}}^{\mathrm{L}}\right) \left|T_{\boldsymbol{q}\mathbf{1}\,\mathbf{23}}^{\mathrm{LU}}\right|^2 \\ \times \left[n_{\mathbf{2}}^{\mathrm{U}} n_{\mathbf{3}}^{\mathrm{U}} \left(n_{\boldsymbol{q}}^{\mathrm{L}} + n_{\mathbf{1}}^{\mathrm{L}}\right) - n_{\boldsymbol{q}}^{\mathrm{L}} n_{\mathbf{1}}^{\mathrm{L}} \left(n_{\mathbf{2}}^{\mathrm{U}} + n_{\mathbf{3}}^{\mathrm{U}}\right)\right] . \end{aligned} \tag{9c}$$

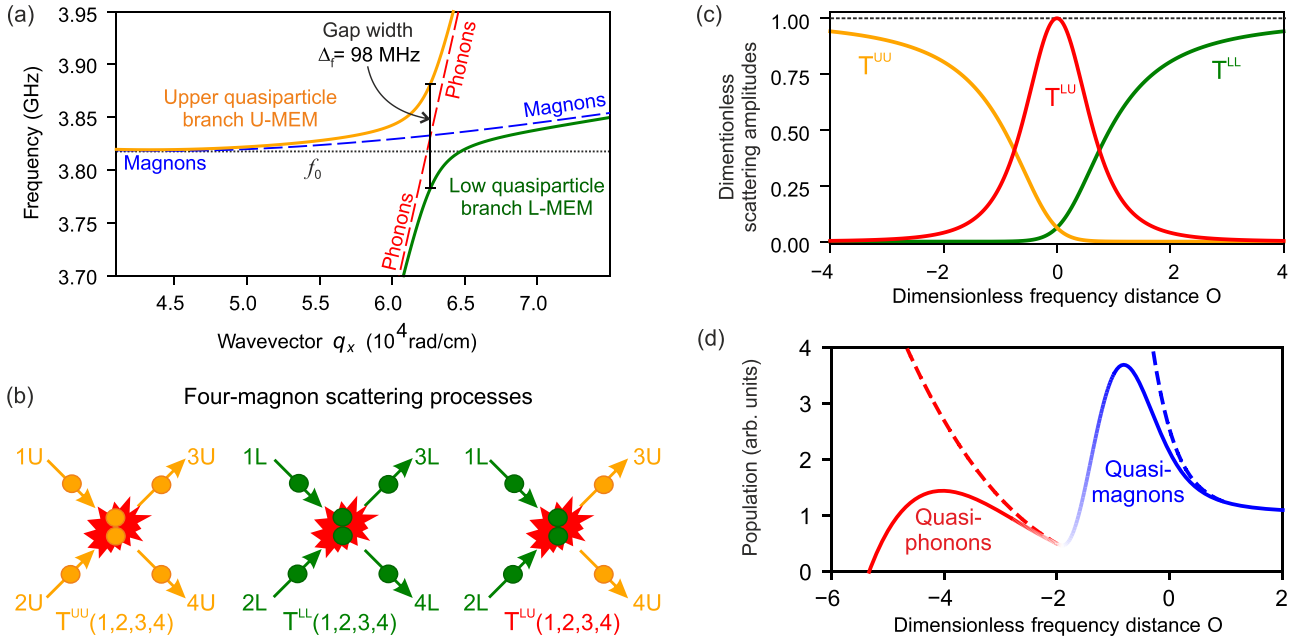

FIG. 5. (a) shows the calculated magnon-phonon spectrum near the hybridization region. (b) gives the schematic representations of the scattering and cross-scattering four-particle processes in the hybridization region. (c) presents squares of interaction amplitudes T_q^{UU}, T_q^{LL} and $4T_q^{\mathrm{LU}}$, normalized by T_q, vs the dimensionless distance from the hybridization crossover O_q. Panel (d): Solutions of balance equations in the cross-section area $-2 < O_\kappa < 2$, (solid blue line) and below the BEC frequency $-2 > O_\kappa$, solid red line. Blue and red dashed lines: particle profiles N_κ^{L} for constant particle fluxes μ_κ^{L} =const.

IV. DOUBLE ACCUMULATION OF HYBRID BOSONS

A full consistent theoretical description of the bottleneck accumulation process of hybrid magnetoelastic bosons, based on the kinetic equation (9) for the actual YIG frequency spectra and the interaction amplitudes, is beyond the scope of this article. In Sec. IV A, for a quantitative understanding of this problem, we restrict ourselves to the simplifying assumption of axial symmetry of the problem in the vicinities of the frequency minima at $\boldsymbol{q} = \pm\boldsymbol{q}_0$. Then, in Sec. V, we turn to a two-dimensional description of the problem, considering caustics in the quasiparticle propagation which results in sharp anisotropic beams.

A. One-dimensional differential model

Denoting $\boldsymbol{\kappa}_\pm = \boldsymbol{q} \mp \boldsymbol{q}_0$ we introduce a one-dimensional approximation of the L- and U-MEM densities

$$N^{\mathrm{L}}_{\kappa_\pm} = 4\pi\kappa_\pm^2 n^{\mathrm{L}}_{\kappa_\pm}\ ,\ N^{\mathrm{U}}_{\kappa_\pm} = 4\pi\kappa_\pm^2 n^{\mathrm{U}}_{\kappa_\pm}\ . \tag{10a}$$

To simplify further the appearance of the equations, we will ignore the difference between the $\pm\boldsymbol{q}_0$ frequency minima and omit the symbol "±". This simplification does not affect the qualitative picture of the described phenomena.

Now we can present the kinetic equation (8) as follows:

$$\frac{\partial N^{\mathrm{L}}_\kappa}{\partial t} = 4\pi\kappa^2\left[\mathrm{St}^{\mathrm{LL}}(\kappa,t) + \mathrm{St}^{\mathrm{LU}}(\kappa,t)\right], \tag{10b}$$

$$\frac{\partial N^{\mathrm{U}}_\kappa}{\partial t} = 4\pi\kappa^2\left[\mathrm{St}^{\mathrm{UU}}(\kappa,t) - \mathrm{St}^{\mathrm{LU}}(\kappa,t)\right]. \tag{10c}$$

B. Estimates of the flux and the L → U transformation rate

The collision terms $\mathrm{St}^{\mathrm{LL}}(\kappa,t)$ and $\mathrm{St}^{\mathrm{UU}}(\kappa,t)$ preserve the total number of quasiparticle in the L-MEM and U-MEM, respectively. Therefore they may be represented in a divergent form, for instance,

$$\mathrm{St}^{\mathrm{LL}}(\kappa,t) = d\mu^{\mathrm{L}}_\kappa/d\kappa\ , \tag{11a}$$

where μ^{L}_κ is the L-MEM particle flux towards small wave numbers. Together with Eq. (11a), this gives

$$\mu^{\mathrm{L}}_\kappa = 4\pi\int^\kappa \kappa^2\mathrm{St}^{\mathrm{LL}}(\kappa')d\kappa'\ . \tag{11b}$$

Now, using Eq. (9b), we obtain an estimate for the flux μ^{L}_q

$$\mu^{\mathrm{L}}_\kappa = a_1\kappa_\times^3\left(T^{\mathrm{LL}}_\kappa\right)^2\left(N^{\mathrm{L}}_\kappa\right)^3/\delta\omega_\kappa\ . \tag{11c}$$

Here $\delta\omega_\kappa \equiv \kappa^2[d^2\omega_q/2(dq)^2]_{q=q_0}$ and $T^{\mathrm{LL}}_\kappa = T_0\cos^4\varphi_\kappa$, with $T_0 = T_{\boldsymbol{q}_0\boldsymbol{q}_0,\boldsymbol{q}_0\boldsymbol{q}_0}$ and $\cos\varphi_\kappa$ given by Eq. (4b) were $\boldsymbol{q} = \boldsymbol{q}_0 + \boldsymbol{\kappa}$. In Eq. (11c) $a_1 \sim 1$, as follows, for example, from Sec. 2.1.4 in Ref. [58]. As it is clear again from Ref. [58], a similar estimate of the collision integral $\mathrm{St}^{\mathrm{LU}}_\kappa = \mathrm{St}^{\mathrm{LU}}(\kappa)$, Eq. (9c), takes the form

$$\mathrm{St}^{\mathrm{LU}}_\kappa = a_2\,\kappa_\times^2\left(T^{\mathrm{LU}}_\kappa\right)^2 N^{\mathrm{L}}_\kappa N^{\mathrm{U}}_\kappa\left(N^{\mathrm{U}}_\kappa - N^{\mathrm{L}}_\kappa\right)/\delta\omega_\kappa\ , \tag{11d}$$

where $T^{\mathrm{LU}}_\kappa = T_0\cos^2\varphi_\kappa\sin^2\varphi_\kappa$. In Eq. (11d), the parameter a_2 includes the same set of estimates, as parameter a_1 in Eq. (11c), e.g., $\delta(\Omega\ldots) \sim 1/\delta\omega_\kappa$. Therefore their ratio can be estimated even better than a_1 and a_2 separately: a_2/a_1 is of the order of unity, say, between 1/3 and 3. It can be shown that conservation laws of frequency and momentum fully forbid the scattering process (11d) when the frequency of the lower

mode becomes smaller than the lowest possible frequency of the upper mode, i.e., the BEC frequency ω_0. It means that the estimate (11d) is valid if $\Omega_\kappa^{\rm L} > \min \Omega_\kappa^{\rm U} = \omega_0$. Otherwise, $\mathrm{St}_\kappa^{\rm LU} = 0$. Note that Eqs. (11c) and (11d) are more accurate than the preliminary estimates given in Ref. [59].

Now, in the stationary case the kinetic equation (10b) for the lower mode can be written as follows:

$$\frac{d\mu_\kappa^{\rm L}}{d\kappa} + \mathrm{St}_\kappa^{\rm LU} = 0\,. \tag{12}$$

C. Rate equation above the BEC frequency

Using estimates (11c) and (11d), we can rewrite the rate Eq. (12) as

$$\frac{d}{d\kappa}\left[\kappa_\times^3 \cos^8\varphi_\kappa \left(\mathcal{N}_\kappa^{\rm L}\right)^3\right] = 3\,a\left(\mathcal{N}_\kappa^{\rm L}\right)^2 \kappa^2 \cos^4\varphi_\kappa \sin^4\varphi_\kappa\,. \tag{13}$$

Here, $a \simeq a_2/a_1 \simeq 1$, the prefactor 3 is chosen to simplify the appearance of the final Eq. (14), $\mathcal{N}_\kappa^{\rm L} = N_\kappa^{\rm L}/N_+^{\rm L}$ is the dimensionless L-MEM density, normalized by the density $N_+^{\rm L}$ at a sufficiently large positive O_κ, say at $O_\kappa = 3$. In Eq. (11d), we assume for simplicity's sake that $N_\kappa^{\rm L} \gg N_\kappa^{\rm U}$ and prescribe $N_\kappa^{\rm U}$ as $\kappa^2 N_+^{\rm L}/\kappa_\times^2$ according to Eq. (10a) with $n_\kappa^{\rm U} = \text{const}$. Further analysis shows that our qualitative results are not sensitive to a particular value of a, confirming the validity of using the chosen value of $a = 3$.

The ordinary differential Eq. (13) can be solved with the boundary condition $\mathcal{N}_\kappa^{\rm L} = 1$ for $\kappa \to \infty$ giving the relative MEMs population in the hybridization region (above the BEC frequency and thus with a plus-symbol)

$$\mathcal{N}_\kappa^{+,\rm L} = \frac{1}{\cos^{8/3}\varphi_\kappa}\left[1 - a\int_{\kappa/\kappa_\times}^{\infty} \frac{x^2 \sin^4\varphi_x dx}{\cos^{4/3}\varphi_x}\right]. \tag{14}$$

In Fig. 5(d), we plot $\mathcal{N}_\kappa^{+,\rm L}$ in red as a function of the dimensionless distance to the crossover O_κ defined by Eq. (4b). For concreteness we took the position of the frequency minimum $\kappa = 0$ as $O_0 = -2$. We see a sharp peak of $\mathcal{N}_O^{+,\rm L}$ demonstrating the bottleneck accumulation of quasimagnons in the hybridization region above the BEC frequency around $O \approx -1$. This peak is a result of the completion of two processes. The first one is the quasiparticle flux towards lower frequencies (negative O), which on its own leads to an infinite growth of $N_O^{+,\rm L}$, shown by the red dashed line in Fig. 5(d). This growth is caused by a decrease in the intrinsic LL nonlinearity [see plot of $T_\kappa^{\rm LL}$ in Fig. 5(d)], which has to be compensated by an increase in $N_O^{+,\rm L}$ to ensure a constant particle flux. This increase of $N_O^{+,\rm L}$ is limited by the second process: the intermodal L → U particle flux, provided by the $\mathrm{St}_\kappa^{\rm LU}$ collision integral (11d). For frequencies of the lower mode $\Omega_\kappa^{\rm L} < \omega_0$ (i.e., below the BEC frequency) $\mathrm{St}_\kappa^{\rm LU}$ becomes zero (by the conservation laws of frequency and momentum) and growth of $N_O^{\rm L}$ reappears, see red dashed line in Fig. 5(d). We consider this effect in Sec. IV D.

D. Rate equation below the BEC frequency

Below the BEC frequency we have $\mathrm{St}_\kappa^{\rm LU} = 0$ (see (12)) and we have to account for another dissipation mechanism able to suppress the infinite growth of $\mathcal{N}_\kappa^{\rm L}$. The simplest option is a small linear damping term $\gamma\mathcal{N}_\kappa^{\rm L}$ originating from three-magnon scattering processes, magnon-phonon interaction, or other processes. With this term instead of Eq. (12), we have

$$\frac{d\mu_\kappa^{\rm L}}{d\kappa} + \gamma\mathcal{N}_\kappa^{\rm LU} = 0\,. \tag{15}$$

Now, using an estimate (11c) we can rewrite rate Eq. (15) similarly to Eq. (13)

$$\frac{d}{d\kappa}\left[\kappa_\times \cos^8\varphi_\kappa \left(\mathcal{N}_\kappa^{\rm L}\right)^3\right] + \frac{3}{2}\widetilde{\gamma}\,\mathcal{N}_\kappa^{\rm L} = 0\,. \tag{16}$$

The dimensionless damping frequency $\widetilde{\gamma} = \gamma/T^{\rm LL}N_+^{\rm L}$ is normalized by the typical nonlinear frequency shift $T^{\rm LL}N_+^{\rm L}$ and can be estimated in our experiments as $\widetilde{\gamma} \sim 10^{-2}$. The solution of the ordinary differential equation (16) with proper boundary conditions at the BEC frequency (i.e., for $\kappa = 0$) provides the relative population of the L-MEM branch for smaller frequencies (minus symbol)

$$\mathcal{N}_\kappa^{-,\rm L} = \mathcal{N}_0^{+,\rm L}\frac{\cos^{8/3}\varphi_0}{\cos^{8/3}\varphi_\kappa}\left(1 - \tilde{\gamma}\int_{\kappa/\kappa_\times}^{0} \frac{dx}{\cos^{4/3}\varphi_x}\right)^{1/2}. \tag{17}$$

In Fig. 5(d), we plot $\mathcal{N}^{-,\rm L}$ by a solid blue line as a function of the dimensionless distance to the crossover O_κ below the BEC frequency (in our case for $O < -2$). For concreteness, we took $\widetilde{\gamma} = 0.01$. We see a second sharp peak of $\mathcal{N}_O^{\rm L}$ demonstrating the bottleneck accumulation of quasiphonons much below the BEC frequency around $O \approx -4$.

V. TWO-DIMENSIONAL MODEL: CAUSTICS AND ANISOTROPIC BEAMS

Above, we formulated a one-dimensional model of the bottleneck accumulation of hybrid magnetoelastic quasiparticles during the thermalization of parametrically pumped magnons. The model predicts the existence of two regions of such accumulation (slow quasimagnons and fast quasiphonons) with frequencies above and below the BEC frequency, $f_{\rm slow} > f_0 > f_{\rm fast}$.

However, we are unable to determine the spectral positions of these peaks quantitatively. The problem is that instead of integration over the wave-vector space we used local estimations (11c) and (11d) of the collision integral (9a). This approximation works more or less reasonably well in hydrodynamic turbulence theory with a large scale-invariant interval in wave-vector space and smooth dependence of interaction amplitudes, as in Ref. [61]. However, this is not the case in our problem: the relevant interaction amplitudes demonstrate a sharp q dependence in the vicinity of the crossover region. Thus a quantitative description of the problem require an explicit solution of the rate equation with the actual form (9a) of the collision integral and realistic boundary conditions.

Moreover, the suggested one-dimensional model leaves the question unanswered about the angular dependence of the propagation directions of the slow and fast quasiparticles, which should be the subject of a full three-dimensional theory. Such a theory must take into account the strongly anisotropic frequency spectrum of magnons and requires knowledge of the three-dimensional population of the L-MEM branch above

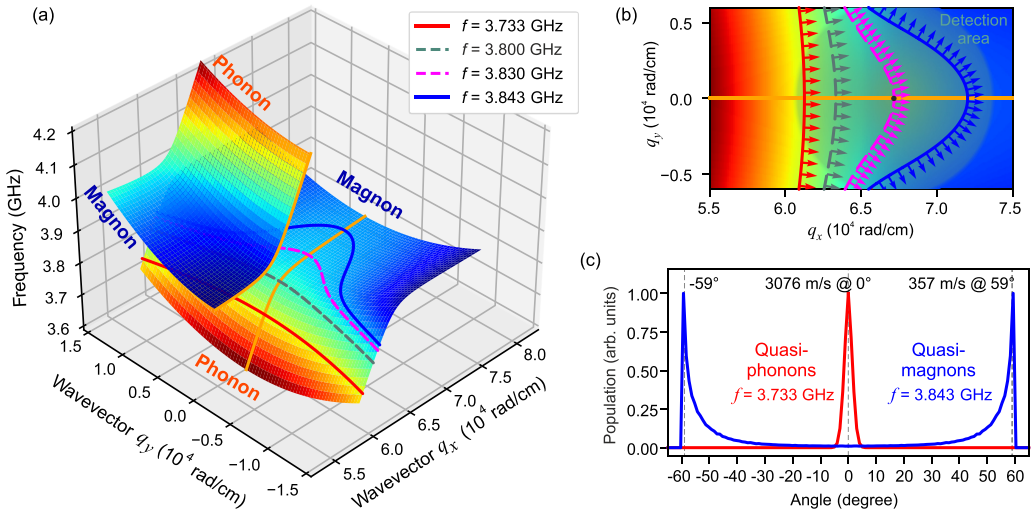

FIG. 6. The graph in panel (a) shows the two-dimensional dispersion of magnetoelastic quasiparticles at the magnon-phonon crossing. The color scale symbolizes the kind of the particle. dark red stands for a pure phonon state, while blue stands for a pure magnon state. Two continuous orange lines mark the dispersion branches with the perpendicular wave vector $q_y = 0$. The red, green, purple, and blue lines are selected isofrequency curves. (b) This panel shows an intensity map of the lower part of the magnon-phonon dispersion shown in (a). The arrows indicate the directions of quasiparticle propagation in different sections of the isofrequency curves, and, by definition of the group velocity, they are always perpendicular to the isofrequency curves. The green shaded area symbolizes the Gaussian response function of the measurement setup in wave-vector space. (c) shows the quasiparticle population along the isofrequency curve in dependence of the propagation angle α. It becomes obvious that each of the shown isofrequency curves has preferred angles and mean velocities of the quasiparticles populating it. These angles increase with growing frequency. The propagation angle of the red curve is nearly 0°, while the blue curve has two angles of $\pm 59°$.

the crossing frequency $f_\times$, and the U-MEM branch from f_0 to $f_\times$ and higher. Neither do we know these distributions experimentally nor theoretically. In this situation, we can only make the simplest assumptions about the mentioned distribution functions and compare the obtained results with the experiment.

Figure 6(a) shows two-dimensional frequency spectra of U- and L-MEMs in the vicinity of the magnon-phonon hybridization area, calculated using the coupled dipole-exchange spin-wave and acoustic wave equations presented in Appendix A. With the solid red line we plotted here the isofrequency curve of fast quasiphonons at 3733 MHz. Its shape looks like a segment of a perfect circle formed by the intersection of the isofrequency plane with the phonon dispersion cone, only slightly distorted by hybridization with the magnon spectrum. The blue solid line shows the isofrequency curve of slow quasimagnons at 3843 MHz. This curve deviates significantly from the circular shape due to the influence of strongly anisotropic magnon dispersion. To more clearly demonstrate the transition between these two curves, we also plotted two intermediate isofrequency curves at 3800 MHz and 3830 MHz as dashed lines. The same four curves are also represented in the (q_x, q_y) plane in Fig. 6(b). They are complemented by arrows indicating the directions of group velocities. The L-MEM quasiparticles belonging to these isofrequency curves have a different primary direction of propagation.

Obviously, the sensitivity of the BLS detection of quasiparticles $S_{\boldsymbol{q}}$ is limited in the (q_x, q_y) space. In our experiment, the center of the area of maximum sensitivity corresponds to the position of the small black circle in Fig. 6(b). When moving away from it, the sensitivity decreases approximately tantamount to a Gaussian curve with a standard deviation of $\sigma \sim 10^3$ rad/cm. A qualitative estimate of the observational region in which we can register quasiparticles is shown as a circle-shaped green area. We see that it includes some part of the red line shown in Fig. 6(b). The group velocities of all corresponding quasiphonons are almost directed along q_x. On the other hand, the quasimagnons belonging to the blue isofrequency curve in the green area of observation can be divided into two groups with positive and negative q_y, above and below the horizontal orange solid line. A substantial fraction of the upper part of the isofrequency curve around the inflection point has almost equally directed group velocities pointing upward at an angle of about 60°, causing the formation of a caustic in the propagating quasiparticle beam. Similarly, the lower part of the isofrequency curve with $q_y < 0$ is responsible for the formation of the second caustic beam propagating at an angle $\alpha = -60°$ with respect to the horizontal line $q_y = 0$.

To qualitatively characterize the distribution of group velocities $\boldsymbol{v}^{\mathrm{L}}_{\mathrm{gr}}(\boldsymbol{q})$ within each L-MEM quasiparticle group registered in our experiments, we must find the product $S_{\boldsymbol{q}} n^{\mathrm{L}}_{\boldsymbol{q}} \boldsymbol{v}^{\mathrm{L}}_{\mathrm{gr}} S(\boldsymbol{q})$ along the corresponding part of the dispersion curve. Unfortunately, we do not know the L-MEM population $n^{\mathrm{L}}_{\boldsymbol{q}}$ and can only assume for simplicity's sake that $n^{\mathrm{L}}_{\boldsymbol{q}} = \mathrm{const}$ in the actual area. The resulting distributions of quasiparticles vs. the group velocity angle are shown in Fig. 6(c), where all plots are normalized to their maximum value for better comparison. We see three sharp peaks: a peak of fast quasiphonons with $\alpha = 0°$ and two peaks of slow quasimagnons with $\alpha \approx \pm 59°$. This perfectly resembles the experimentally measured direction of propagation of slow and fast quasiparticles. By extracting the velocities for the points

TABLE I. Characteristic values of the problem determined from the two-dimensional model.

	Fast quasiphonons	Slow quasimagnons	BEC minima	Crossing point
f (MHz)	3733	3843	3819	3833
$q_x\left(\frac{\text{rad}}{\text{cm}}\right)$	61415	67670	43360	62620
$q_y\left(\frac{\text{rad}}{\text{cm}}\right)$	0	±4600	0	0
$v_{\text{gr}}^{\text{theor}}\left(\frac{\text{m}}{\text{s}}\right)$	3076	357	0	–
$v_{\text{gr}}^{\text{exp}}\left(\frac{\text{m}}{\text{s}}\right)$	3070	368	0	–

on the isofrequency curves matching to propagation angles $\alpha = 0^\circ$ and $\pm 59^\circ$, it becomes possible to calculate the average propagation velocity values $v_{\text{gr}}^{\text{theor}}$ for both propagation angles. The results are $v_{\text{gr}}^{\text{theor}}(0^\circ, 3733\ \text{MHz}) = 3076$ m/s and $v_{\text{gr}}^{\text{theor}}(59^\circ, 3843\ \text{MHz}) = 357$ m/s, which are in good agreement with our experimental data [62] (see Table I).

Using the two-dimensional dispersion dependency for the L-MEM spectral branch, we can determine the frequency areas corresponding to the measured group velocities of the slow and fast quasiparticle groups. Figure 7 shows these areas as red and blue stripes for the fast and the slow quasiparticles, respectively. The stripe widths account for the corresponding experimental errors in the group velocities. The intersection of these bands with the $f_{\text{fast}} = 3733$ MHz and $f_{\text{slow}} = 3843$ MHz isofrequency curves determine the directions of predominant propagation of the fast and slow quasiparticles, respectively. The dashed orange line is an isofrequency curve at the magnon BEC frequency f_0. As one can see, this curve lies between the red and blue stripes without crossing them anywhere and being substantially remote from the areas of their intersection with the f_{slow} and f_{fast} isofrequency curves. This indicates that the resultant condition $f_{\text{slow}} > f_0 > f_{\text{fast}}$ for the frequency positions of the quasimagnon and quasiphonon density peaks obtained from our model is well satisfied in the experiment.

One should distinguish a somewhat different nature of the directed quasiparticle fluxes for angles of 59° and 0°. In the first case, the isofrequency curve has two inflections at the points ($q_x \approx 67670$ rad/cm, $q_y \approx \pm 4600$ rad/cm); in their vicinity, canonical caustic patterns are formed [43]. Such caustics are protected from diffraction broadening and have

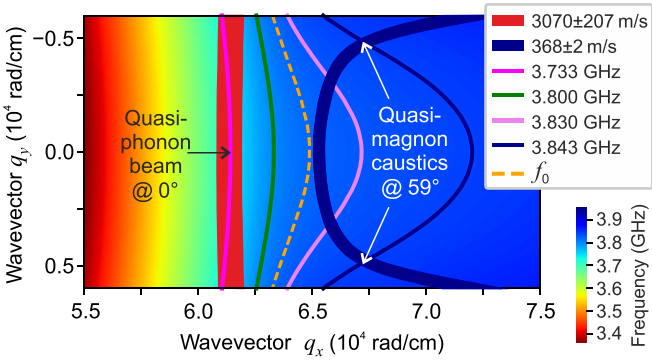

FIG. 7. The frequency regions corresponding to the experimentally measured group velocities of the slow (blue stripe) and fast (red stripe) quasiparticle groups. The dashed orange isofrequency curve relates to the magnon BEC frequency f_0.

a stable transverse aperture, which can be of subwavelength size [44]. In the second case, there are no inflection points and, thus, a conventional weakly divergent beam is formed by quasiparticles with approximately codirected group velocities [63].

It should be noted that any isofrequency curve lying between the blue and red curves, being populated, should form either focused or caustic beams at some propagation angles in the range from 0 to ±59°. In our experiment, however, we do not observe quasiparticle propagation between these two boundary cases. This fact convincingly confirms the model of double accumulation of magnetoelastic bosons in the magnon-phonon hybridization region.

VI. DISCUSSION AND SUMMARY

We experimentally showed the appearance of two groups of hybrid magnetoelastic modes at the bottom of the spectrum of a parametrically overpopulated magnon gas in an in-plane magnetized magnetic film. These two groups form spatially separated beams with different group velocities. The first—"slow"—group propagates with velocity $v_{\text{slow}} \approx 368$ m/s under the angles $\alpha_{\text{slow}} \approx \pm 59^\circ$ with respect to the external magnetic field $\boldsymbol{H} \| \hat{\boldsymbol{x}}$. The second—"fast"—group appears later and propagates with velocity $v_{\text{fast}} \approx 3070$ m/s along $\hat{\boldsymbol{x}}$: $\boldsymbol{v}_{\text{fast}} \| \boldsymbol{H} \| \hat{\boldsymbol{x}}$.

We formulated a simple one-dimensional model of the bottleneck accumulation of hybrid MEMs during the process of parametrically pumped magnons evolution toward their Bose-Einstein condensation. The model predicts two accumulation areas (slow quasimagnons and fast quasiphonons) with the frequencies above and below the BEC frequency, $f_{\text{slow}} > f_0 > f_{\text{fast}}$, exactly as observed in experiments.

On a qualitative level, the emergence of these two accumulation areas can be undersood as follows. Short-wavelength magnons parametrically pumped to the upper magnon-phonon dispersion branch scatter through a step-by-step thermalization process towards the bottom of the spin-wave spectrum. As the magnon-phonon hybridization region is approached, the efficiency of nonlinear scattering decreases, and, consequently, the downward quasiparticle flux slows down. Such a deceleration causes the formation of a quasimagnon density peak owing to the bottle-neck effect. The intensity of this peak saturates due to the scattering of quasimagnons to the lower branch of the magnon-phonon spectrum, where they, moving away from the hybridization region, regain their magnetic character and take part in the formation of the magnon condensate. The remaining quasimagnons, continuing to scatter toward entirely linear phonon states below the magnon spectrum, transform into quasiphonons with vanishing scattering amplitude. Without being able to transfer into another mode, they form a second peak in the quasiparticle density. This peak saturates due to the natural decay of quasiphonons.

We consider the qualitative agreement of the experimental results with the simple analytical model as a strong evidence that our one-dimensional model grasps adequately the basic physics of the bottleneck accumulation phenomenon in the frequency domain.

To explain the reason for the observed slow and fast quasiparticle propagation in narrow angular intervals around

$\alpha_{\text{slow}}^{\text{exp}} \approx \pm 59^\circ$ and $\alpha_{\text{fast}}^{\text{exp}} \approx 0^\circ$ we considered in Sec. V two-dimensional frequency spectra and found well-defined regions with almost the same group velocities–caustics–around the inflection points in the BLS registered part of the $\boldsymbol{q}$-space. Using only this knowledge, we theoretically found propagation angles $\alpha_{\text{slow}}^{\text{theor}} = \pm 59^\circ$ and $\alpha_{\text{fast}}^{\text{theor}} = 0^\circ$ [see Fig. 6(c)], which perfectly agree with corresponding experimental values $\alpha_{\text{slow}}^{\text{exp}} \approx \pm 59^\circ$ and $\alpha_{\text{fast}}^{\text{exp}} \approx 0^\circ$.

We consider the discovered double accumulation of magnetoelastic modes with nonzero group velocities as a promising effect for applications in future magnon spintronic devices. To determine the specific field of such applications, one should clarify the degree of real spectral localization of each of these quasiparticle groups and, consequently, the degree of their coherence. We believe that the answer to this question can be obtained by interference experiments with accumulated quasiparticles.

ACKNOWLEDGMENTS

Financial support by the European Research Council within the Advanced Grant 694709 SuperMagnonics – "Supercurrents of Magnon Condensates for Advanced Magnonics" as well as financial support by the Deutsche Forschungsgemeinschaft (DFG, German Research Foundation) through the Collaborative Research Center "Spin+X: Spin in its collective environment" TRR – 173 – 268565370 (project B04) is gratefully acknowledged.

APPENDIX

In the present paper, the magnon-phonon dispersion was calculated based on the theory presented in Refs. [64,65]. The equations given below show a general approach to the problem, and their complete solution is beyond the scope of this Appendix. A detailed derivation of the magnetoelastic spectrum can be found in Ref. [10].

In order to study magnetoelastic waves, both magnetic and elastic equations of motions need to be considered. These individual equations of motion are coupled by introducing a magnetoelastic interaction, so that the elastic displacement $\mathbf{u} = (u_x, u_y, u_z)$ influences the magnetization $\mathbf{M} = (M_x, M_y, M_z)$ and vice versa. The strength of the coupling is defined by the magnetoelastic parameters of bulk YIG: $B_1 = 3.48 \times 10^5\ \mathrm{J\,m^{-3}}$ and $B_2 = 6.96 \times 10^5\ \mathrm{J\,m^{-3}}$. To obtain the equation of motion, it is necessary to introduce an effective field of the magnetoelastic interaction into the Landau-Lifshitz equation and insert a magnetoelastic force into the mechanical equations of motions. We end up with the following five coupled differential equations, starting with the magnetic equations:

$$\frac{1}{\gamma}\frac{\partial M_x}{\partial t} = -\frac{B_2}{M_0}\left(\frac{\partial u_y}{\partial x} + \frac{\partial u_x}{\partial y}\right)M_x - \left[H_{\text{eff},z} - D\nabla^2 + 2\frac{B_1}{M_0}\left(\frac{\partial u_y}{\partial y} - \frac{\partial u_z}{\partial z}\right)\right]M_y + H_{\text{eff},y}M_z - B_2\left(\frac{\partial u_z}{\partial y} + \frac{\partial u_y}{\partial z}\right), \quad \text{(A1a)}$$

$$\frac{1}{\gamma}\frac{\partial M_y}{\partial t} = \frac{B_2}{M_0}\left(\frac{\partial u_y}{\partial x} + \frac{\partial u_x}{\partial y}\right)M_y + \left[H_{\text{eff},z} - D\nabla^2 + 2\frac{B_1}{M_0}\left(\frac{\partial u_x}{\partial x} - \frac{\partial u_z}{\partial z}\right)\right]M_x - H_{\text{eff},x}M_z + B_2\left(\frac{\partial u_z}{\partial x} + \frac{\partial u_x}{\partial z}\right). \quad \text{(A1b)}$$

The equations are derived under the assumption that a strong external magnetic field is applied along the z axes. Therefore we can assume that the magnetic moments along x and y are small compared to M_z, so that $M_z \gg M_x, M_y$ with $M_z \approx M_0 = \sqrt{M_x^2 + M_y^2 + M_z^2}$. This assumption allows us to neglect second order terms of the magnetization $M_i M_j$ with $i, j \in [x, y]$ and set $M_z/M_0 = 1$. The third equation is not shown because the magnetization component M_z can be determined if the length of the total magnetization vector $\mathbf{M}$ is conserved. The effective field H_{eff} involves the magnetic fields, both steady and ac, as well as the dipole-dipole field and the effective anisotropy field. Here are the three elastic equations:

$$\rho\frac{\partial^2 u_x}{\partial t^2} = c_{44}\nabla^2 u_x + (c_{44} + c_{12})\frac{\partial}{\partial x}\text{div}\,\mathbf{u} + \frac{B_1}{M_0^2}\frac{\partial M_x^2}{\partial x} + \frac{B_2}{M_0^2}\left[\frac{\partial}{\partial y}(M_x M_y) + \frac{\partial}{\partial z}(M_x M_z)\right], \quad \text{(A2a)}$$

$$\rho\frac{\partial^2 u_y}{\partial t^2} = c_{44}\nabla^2 u_y + (c_{44} + c_{12})\frac{\partial}{\partial y}\text{div}\,\mathbf{u} + \frac{B_1}{M_0^2}\frac{\partial M_y^2}{\partial y} + \frac{B_2}{M_0^2}\left[\frac{\partial}{\partial z}(M_y M_z) + \frac{\partial}{\partial x}(M_y M_x)\right], \quad \text{(A2b)}$$

$$\rho\frac{\partial^2 u_z}{\partial t^2} = c_{44}\nabla^2 u_z + (c_{44} + c_{12})\frac{\partial}{\partial z}\text{div}\,\mathbf{u} + \frac{B_1}{M_0^2}\frac{\partial M_z^2}{\partial z} + \frac{B_2}{M_0^2}\left[\frac{\partial}{\partial x}(M_z M_x) + \frac{\partial}{\partial y}(M_z M_y)\right], \quad \text{(A2c)}$$

where $\rho = 5.17\ \mathrm{g/cm^3}$ is the density of YIG. The elastic stiffness constants c_{44}, c_{12} define the mechanical strain on the material.

Restricting ourselves to a cubic ferromagnet magnetized to saturation along the $\langle 001 \rangle$ axis it is possible to derive the dispersion law by substitution of $M_{x,y} = m_{0(x,y)}\exp i(\omega t - \mathbf{qr})$ and $u_{x,y,z} = u_{0(x,y,z)}\exp i(\omega t - \mathbf{qr})$ in equations (A1,A2)

$$i\omega m_x^0 + \omega_{mag} m_y^0 - i\gamma q B_2 u_y^0 = 0, \quad i\omega m_y^0 - \omega_{mag} m_x^0 + i\gamma q B_2 u_x^0 = 0, \quad (\omega^2\rho - q^2 c_{44})u_x^0 - iq\frac{B_2}{M_0}m_x^0 = 0,$$

$$(\omega^2\rho - q^2 c_{44})u_y^0 - iq\frac{B_2}{M_0}m_y^0 = 0, \quad \text{(A3)}$$

$$(\omega^2\rho - q^2 c_{11})u_z^0 = 0\,, \quad \text{(A4)}$$

where ω_{mag} is the pure magnon dispersion [65] in the region of the hybridization. The numerical solution of this system provides the hybridized magnon-phonon dispersions shown in Fig. 1. Equation (A4) is decoupled from the others and describes a pure elastic longitudinal wave with linear dispersion relation, which does not interact with the magnetic subsystem in our geometry.

[1] L. Venema, B. Verberck, I. Georgescu, G. Prando, E. Couderc, S. Milana, M. Maragkou, L. Persechini, G. Pacchioni, and L. Fleet, The quasiparticle zoo, Nat. Phys. **12**, 1085 (2016).

[2] F. J. Dyson, General theory of spin-wave interactions, Phys. Rev. **102**, 1217 (1956).

[3] A. Einstein, Die Plancksche Theorie der Strahlung und die Theorie der spezifischen Wärme, Ann. Phys. **22**, 180 (1907).

[4] H. F. Tiersten, Coupled magnetomechanical equations for magnetically saturated insulators, J. Math. Phys. **5**, 1298 (1964).

[5] T. Kobayashi, R. C. Barker, J. L. Bleustein, and A. Yelon, Ferromagnetoelastic resonance in thin films. I. Formal treatment, Phys. Rev. B **7**, 3273 (1973).

[6] T. Kobayashi, R. C. Barker, and A. Yelon, Ferromagnetoelastic resonance in thin films. II. Application to Nickel, Phys. Rev. B **7**, 3286 (1973).

[7] H. Bömmel and K. Dransfeld, Excitation of Hypersonic Waves by Ferromagnetic Resonance, Phys. Rev. Lett. **3**, 83 (1959).

[8] M. Pomerantz, Excitation of Spin-Wave Resonance by Microwave Phonons, Phys. Rev. Lett. **7**, 312 (1961).

[9] S. M. Rezende and F. R. Morgenthaler, Magnetoelastic waves in time-varying magnetic fields. I. Theory, J. Appl. Phys. **40**, 524 (1969).

[10] A. Rückriegel, P. Kopietz, D. A. Bozhko, A. A. Serga, and B. Hillebrands, Magnetoelastic modes and lifetime of magnons in thin yttrium iron garnet films, Phys. Rev. B **89**, 184413 (2014).

[11] T. Kikkawa, K. Shen, B. Flebus, R. A. Duine, K. I. Uchida, Z. Qiu, G. E. W. Bauer, and E. Saitoh, Magnon Polarons in the Spin Seebeck Effect, Phys. Rev. Lett. **117**, 207203 (2016).

[12] V. G. Baryakhtar and A. G. Danilevich, Magnetoelastic oscillations in ferromagnets with cubic symmetry, Low Temp. Phys. **43**, 351 (2017).

[13] D. A. Bozhko, V. I. Vasyuchka, A. V. Chumak, and A. A. Serga, Magnon-phonon interactions in magnon spintronics (Review article), Low Temp. Phys. **46**, 383 (2020).

[14] A. G. Olabi and A. Grunwald, Design and application of magnetostrictive materials, Materials and Design **29**, 469 (2008).

[15] A. V. Chumak, P. Dhagat, A. Jander, A. A. Serga, and B. Hillebrands, Reverse Doppler effect of magnons with negative group velocity scattered from a moving Bragg grating, Phys. Rev. B **81**, 140404(R) (2010).

[16] J. P. Domann, C. M. Loeffler, B. E. Martin, and G. P. Carman, High strain-rate magnetoelasticity in Galfenol, J. Appl. Phys. **118**, 123904 (2015).

[17] A. Kamra, H. Keshtgar, P. Yan, and G. E. W. Bauer, Coherent elastic excitation of spin waves, Phys. Rev. B **91**, 104409 (2015).

[18] S. C. Guerreiro and S. M. Rezende, Magnon-phonon interconversion in a dynamically reconfigurable magnetic material, Phys. Rev. B **92**, 214437 (2015).

[19] R. G. Kryshtal and A. V. Medved, Nonlinear spin waves in dynamic magnonic crystals created by surface acoustic waves in yttrium iron garnet films, J. Phys. D. Appl. Phys. **50**, 495004 (2017).

[20] K. An, A. N. Litvinenko, R. Kohno, A. A. Fuad, V. V. Naletov, L. Vila, U. Ebels, G. de Loubens, H. Hurdequint, N. Beaulieu, J. Ben Youssef, N. Vukadinovic, G. E. W. Bauer, A. N. Slavin, V. S. Tiberkevich, and O. Klein, Coherent long-range transfer of angular momentum between magnon Kittel modes by phonons, Phys. Rev. B **101**, 060407(R) (2020).

[21] C. Zhao, Y. Li, Z. Zhang, M. Vogel, J. E. Pearson, J. Wang, W. Zhang, V. Novosad, Q. Liu, and A. Hoffmann, Phonon Transport Controlled by Ferromagnetic Resonance, Phys. Rev. Appl. **13**, 054032 (2020).

[22] M. Geilen, F. Kohl, A. Nicoloiu, A. Müller, B. Hillebrands, and P. Pirro, Interference of co-propagating Rayleigh and Sezawa waves observed with micro-focused Brillouin light scattering spectroscopy, Appl. Phys. Lett. **117**, 213501 (2020).

[23] L. Dreher, M. Weiler, M. Pernpeintner, H. Huebl, R. Gross, M. S. Brandt, and S. T. B. Goennenwein, Surface acoustic wave driven ferromagnetic resonance in nickel thin films: Theory and experiment, Phys. Rev. B **86**, 134415 (2012).

[24] C. Kittel, Interaction of spin waves and ultrasonic waves in ferromagnetic crystals, Phys. Rev. **110**, 836 (1958).

[25] W. Strauss, Elastic and magnetoelastic waves in yttrium iron garnet, Proc. IEEE **53**, 1485 (1965).

[26] R. E. Camley and R. Q. Scott, Surface magnetoelastic waves in the presence of exchange interactions and pinning of surface spins, Phys. Rev. B **17**, 4327 (1978).

[27] R. E. Camley, Magnetoelastic waves in a ferromagnetic film on a nonmagnetic substrate, J. Appl. Phys. **50**, 5272 (1979).

[28] K. Shen and G. E. W. Bauer, Laser-induced Spatiotemporal dynamics of Magnetic Films, Phys. Rev. Lett. **115**, 197201 (2015).

[29] A. Kamra and G. E. W. Bauer, Actuation, propagation, and detection of transverse magnetoelastic waves in ferromagnets, Solid State Commun. **198**, 35 (2014).

[30] N. Ogawa, W. Koshibae, A. J. Beekman, N. Nagaosa, M. Kubota, M. Kawasaki, and Y. Tokura, Photodrive of magnetic bubbles via magnetoelastic waves, Proc. Natl. Acad. Sci. USA **112**, 8977 (2015).

[31] Y. Hashimoto, S. Daimon, R. Iguchi, Y. Oikawa, K. Shen, K. Sato, D. Bossini, Y. Tabuchi, T. Satoh, B. Hillebrands, G. E. W. Bauer, T. H. Johansen, A. Kirilyuk, Th. Rasing, and E. Saitoh, All-optical observation and reconstruction of spin wave dispersion, Nat. Commun. **8**, 15859 (2017).

[32] M. Küß, M. Heigl, L. Flacke, A. Hörner, M. Weiler, M. Albrecht, and A. Wixforth, Nonreciprocal Dzyaloshinskii-Moriya Magnetoacoustic Waves, Phys. Rev. Lett. **125**, 217203 (2020).

[33] D. A. Bozhko, P. Clausen, G. A. Melkov, V. S. L'vov, A. Pomyalov, V. I. Vasyuchka, A. V. Chumak, B. Hillebrands, and A. A. Serga, Bottleneck Accumulation of Hybrid Magnetoelastic Bosons, Phys. Rev. Lett. **118**, 237201 (2017).

[34] A. S. Sukhanov, M. S. Pavlovskii, Ph. Bourges, H. C. Walker, K. Manna, C. Felser, and D. S. Inosov, Magnon-polaron ex-

citations in the noncollinear antiferromagnet Phys. Rev. B **99**, 214445 (2019).
[35] R. Yahiro, T. Kikkawa, R. Ramos, K. Oyanagi, T. Hioki, S. Daimon, E. Saitoh, Magnon polarons in the spin Peltier effect, Phys. Rev. B **101**, 024407 (2020).
[36] H. Hayashi and K. Ando, Spin Pumping Driven by Magnon Polarons, Phys. Rev. Lett. **121**, 237202 (2018).
[37] R. Ramos, T. Hioki, Y. Hashimoto, T. Kikkawa, P. Frey, A. J. E. Kreil, V. I. Vasyuchka, A. A. Serga, B. Hillebrands, and E. Saitoh, Room temperature and low-field resonant enhancement of spin Seebeck effect in partially compensated magnets, Nat. Commun. **10**, 1 (2019).
[38] B. Flebus, K. Shen, T. Kikkawa, K. I. Uchida, Z. Qiu, E. Saitoh, R. A. Duine, and G. E. W. Bauer, Magnon-polaron transport in magnetic insulators, Phys. Rev. B **95**, 144420 (2017).
[39] A. Rückriegel and R. A. Duine, Long-range Phonon Spin transport in ferromagnet-nonmagnetic Insulator Heterostructures, Phys. Rev. Lett. **124**, 117201 (2020).
[40] J. Holanda, D. S. Maior, O. A. Santos, A. Azevedo, and S. M. Rezende, Evidence of Phonon Pumping by magnonic Spin Currents, Appl. Phys. Lett. **118**, 022409 (2021).
[41] S. O. Demokritov, V. E. Demidov, O. Dzyapko, G. A. Melkov, A. A. Serga, B. Hillebrands, and A. N. Slavin, Bose-Einstein condensation of quasiequilibrium magnons at room temperature under pumping, Nature **443**, 430 (2006).
[42] A. A. Serga, V. S. Tiberkevich, C. W. Sandweg, V. I. Vasyuchka, D. A. Bozhko, A. V. Chumak, T. Neumann, B. Obry, G. A. Melkov, A. N. Slavin, and B. Hillebrands, Bose-Einstein condensation in an ultra-hot gas of pumped magnons, Nat. Commun. **5**, 3452 (2014).
[43] V. Veerakumar and R. E. Camley, Magnon focusing in thin ferromagnetic films, Phys. Rev. B **74**, 214401 (2006).
[44] T. Schneider, A. A. Serga, A. V. Chumak, C. W. Sandweg, S. Trudel, S. Wolff, M. P. Kostylev, V. S. Tiberkevich, A. N. Slavin, and B. Hillebrands, Nondiffractive Subwavelength Wave Beams in a Medium with Externally Controlled Anisotropy, Phys. Rev. Lett. **104**, 197203 (2010).
[45] J. Holanda, D. S. Maior, A. Azevedo, and S. M. Rezende, Detecting the phonon spin in magnon-phonon conversion experiments, Nat. Phys. **14**, 500–506 (2018).
[46] T. Hioki, Y. Hashimoto, and E. Saitoh, Bi-reflection of spin waves, Comm. Phys. **3**, 188 (2020)
[47] F. Heussner, M. Nabinger, T. Fischer, T. Brächer, A. A. Serga, B. Hillebrands, and P. Pirro, Frequency-division multiplexing in magnonic logic networks based on caustic-like spin-wave beams, Phys. Status Solidi RRL **12**, 1800409 (2018).
[48] R. Mock, B. Hillebrands, and R. Sandercock, Construction and performance of a Brillouin scattering set-up using a triple-pass tandem Fabry-Pérot interferometer, J. Phys. E: Sci. Instrum. **20**, 656–659 (1987).
[49] C. W. Sandweg, M. B. Jungfleisch, V. I. Vasyuchka, A. A. Serga, P. Clausen, H. Schultheiss, B. Hillebrands, A. Kreisel, and P. Kopietz, Wide-range wavevector selectivity of magnon gases in Brillouin light scattering spectroscopy, Rev. Sci. Instrum. **81**, 073902 (2010).
[50] D. A. Bozhko, H. Yu. Musiienko-Shmarova, V. S. Tiberkevich, A. N. Slavin, I. I. Syvorotka, B. Hillebrands, and A. A. Serga, Unconventional spin currents in magnetic films, Phys Rev. Res. **2**, 023324 (2020).
[51] O. Büttner, M. Bauer, S. O. Demokritov, B. Hillebrands, Y. S. Kivshar, V. Grimalsky, Yu. Rapoport, and A. N. Slavin, Linear and nonlinear diffraction of dipolar spin waves in yttrium iron garnet films observed by space- and time-resolved Brillouin light scattering, Phys. Rev. B **61**, 11576 (2000).
[52] The software control and laboratory automation was implemented in close collaboration with *THATec Innovation GmbH*.
[53] V. Cherepanov, I. Kolokolov, and V. S. L'vov, The saga of YIG: Spectra, thermodynamics, interaction and relaxation of magnons in a complex magnet, Phys. Rep. **229**, 81 (1993).
[54] V. S. L'vov, *Wave Turbulence Under Parametric Excitations (Applications to Magnetics)* (Springer, Berlin-Heidelberg, 1994).
[55] A. A. Serga, C. W. Sandweg, V. I. Vasyuchka, M. B. Jungfleisch, B. Hillebrands, A. Kreisel, P. Kopietz, and M. P. Kostylev Brillouin light scattering spectroscopy of parametrically excited dipole-exchange magnons, Phys. Rev. B **86**, 134403 (2012).
[56] D. A. Bozhko, A. J. E. Kreil, H. Y. Musiienko-Shmarova, A. A. Serga, A. Pomyalov, V. S. L'vov, and B. Hillebrands, Bogoliubov waves and distant transport of magnon condensate at room temperature, Nat. Commun. **10**, 2460 (2019).
[57] J. J. More, *The Levenberg-Marquardt Algorithm: Implementation and Theory, Numerical Analysis*, edited by G. A. Watson, in Lecture Notes in Mathematics Vol. 630 (Springer, Berlin-Heidelberg, 1977).
[58] V. E. Zakharov, V. S. L'vov, and G. E. Falkovich, *Spectra of Turbulence (Wave Turbulence)* (Springer, Berlin-Heidelberg, 1992).
[59] D. A. Bozhko, P. Clausen, G. A. Melkov, V. S. L'vov, A. Pomyalov, V. I. Vasyuchka, A. V. Chumak, B. Hillebrands, and A. A. Serga, Bottleneck accumulation of hybrid magneto-elastic bosons, arXiv:1612.05925 (2017).
[60] W. Strauss, Magnetoelastic Properties of Yttrium-Iron Garnet, Physical Acoustics **4**, 211 (1968).
[61] V. L'vov and A. Pomyalov, Theory of energy spectra in superfluid ^{4}He counterflow turbulence, Phys. Rev. B. **97**, 214513 (2018).
[62] The errors in determining the frequencies of quasiphonons (3076 ± 20 MHz) and quasimagnons (3843 ± 2 MHz) are estimated as the ranges of frequencies for which the calculated values and directions of the group velocities simultaneously correspond to their experimental values, taking into account the corresponding measurement errors.
[63] F. Heussner, G. Talmelli, M. Geilen, B. Heinz, T. Brächer, F. Ciubotaru, C. Adelmann, K. Yamamoto, A. A. Serga, B. Hillebrands, and P. Pirro, Experimental realization of a passive gigahertz frequency-division demultiplexer for magnonic logic networks, Phys. Status Solidi RRL **14**, 1900695 (2020).
[64] A. G. Gurevich and G. A. Melkov, *Magnetization Oscillations and Waves* (CRC Press, New York, 1996).
[65] B. A. Kalinikos and A. N. Slavin, Theory of dipole-exchange spin wave spectrum for ferromagnetic films with mixed exchange boundary conditions J. Phys. C Solid State Phys. 19 7013 (1986)